

Aerodynamic characteristics of carriage arm equipped on hard magnetic disks

Shigehiko Kaneko · Takashi Nishihara ·
Tatsuo Watanabe

Received: 30 June 2006 / Accepted: 21 November 2006 / Published online: 4 January 2007
© Springer-Verlag 2006

Abstract In order to study aerodynamic characteristics of a carriage arm equipped on hard disk drives, water tunnel tests with ten times enlarged models of an actual arm were conducted based on Reynolds number similitude, which allows the time scale of the phenomena about 1,300 times slower than that compared with the phenomena under actual operation condition in the air. In the tests, flow visualization around the arm model with fluorescent dye injection and laser-light sheet technique was carried out. Fluid dynamic drag, lift and torque on the model were also measured. The effects of the oncoming flow velocity and profile, the installation angle and position of the arm and the configuration of the trailing edge of the arm on the power spectral density of the fluid dynamic force were investigated. As a result, predominant spectrum peak, the Strouhal number of which is about 0.24, is found in the power spectral density of dynamic lift force on the arm. The flow visualization confirmed that the dynamic lift with the spectral peak originates from the alternating vortex shedding from the trailing edge of the arm. The peak rapidly decreases as the installation angle increases while the velocity profile of oncoming

flow and the position of the arm in the gap direction have little effect on the peak component. Furthermore, it was demonstrated that the dynamic lift can be reduced by modification of trailing edge shape of the arm.

1 Introduction

Higher accuracy of positioning control of head stack assembly, which consists of sliders, suspensions and carriage arms, is required in order to achieve higher recording density of hard disk drive (HDD) for information storage device and higher rotation speed of the disks is also required to improve data access speed. In HDD systems, carriage arms are subjected to high-speed air flow induced by high-speed disk rotation, and the aerodynamic force on the arms possibly disturbs the positioning control. Therefore, characteristics of the aerodynamic force acting on the arm, and its arm position and configuration dependency should be identified to suppress excessive vibration of the arm induced by the aerodynamic force.

Structural characteristics of head stack assembly have been investigated by several researchers such as Jiang and Miles (1999), Xu and Guo (2003), Gao et al. (2006), and so on. Kubotera et al. (2002), Tsuda et al. (2003), Shimizu et al. (2003) have conducted numerical simulations to investigate flow structure around a carriage arm and the aerodynamic characteristics concerning 3.5 in. HDDs. These results of numerical simulations, however, have not been verified adequately since actual measurements of them have rarely been conducted. One of the reasons for this is that the

2006 ASME/JSME Joint conference on micromechatronics for information and precision equipment.

S. Kaneko (✉) · T. Watanabe
Department of Mechanical Engineering,
The University of Tokyo, 7-3-1 Hongo, Bunkyo-ku,
Tokyo 113-8656, Japan
e-mail: kaneko@mech.t.u-tokyo.ac.jp

T. Nishihara
Civil Engineering Research Laboratory,
Central Research Institute of Electric Power Industry,
1646 Abiko, Abiko-shi, Chiba 270-1194, Japan

dominant frequencies of unsteady flow phenomena around the arm are expected so high that the phenomena are practically impossible to be measure and observed in the actual HDDs.

In this study, we introduced new method making use of water tunnel test with ten times enlarged model of an actual carriage arm under Reynolds number similitude, which allows the time scale of the phenomena about 1,300 times slower than that compared with the phenomena under actual operation condition in the air. In the series of experiments, flow visualization and unsteady fluid force measurement were simultaneously done and the effects of the oncoming flow velocity and profile, the installation angle and position, the configuration of the trailing edge of the arm on the power spectral density of the bending moment in the lift direction are investigated.

2 Experimental setup

2.1 Actual condition and experimental condition based on Reynolds number similitude

The system under study is schematically described in Fig. 1. A carriage arm is installed in the gap between two 3.5 in. disks and is subjected to the air flow induced

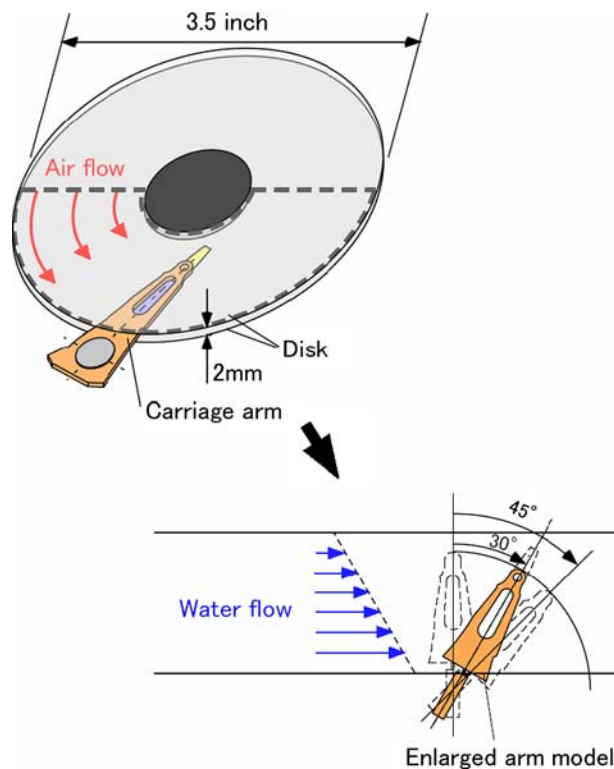


Fig. 1 Carriage arm subjected to flow

by disk rotation. The width of the gap is 2 mm and the thickness of the arm is 1 mm in the actual HDDs. The reference speed of disk rotation is 40 m/s. The feature of the flow around the arm depends principally on Reynolds number Re , which expresses the ratio of fluid forces of inertia and viscosity and is defined as follows:

$$Re = \frac{Ud}{\nu},$$

where U , d and ν denote reference flow velocity, arm thickness and kinematic viscosity of fluid, respectively. The effect of compressibility and variation of fluid density is considered negligible.

In the present water experiments, a ten times larger model of an actual carriage arm is used and is installed in a horizontal and rectangular flow tunnel with a 20 mm height and a 320 mm width. Flow visualization around the arm and measurement of fluid dynamic force on the arm were conducted in the present experiments. Comparison between the actual and experimental conditions is summarized in Table 1, where we can find that Reynolds similitude is realized in the present experimental system. It is notable that the reference time scale of flow phenomenon in the experiments is about 1,300 times slower than that under actual condition in the air since the time scale is proportional to d/U , which enables us to observe the flow around the arm model in detail. Similar method was used by Eguchi et al. (1998, 2002) to observe surface flow around a conductor for overhead electric transmission lines.

It is also notable that the fluid force measured in the water experiments can be reduced to that in the air flow in the actual HDDs as follows:

$$\begin{aligned} F_a &= F_w \frac{\rho_a U_a^2 d_a^2}{\rho_w U_w^2 d_w^2} \\ &= F_w \frac{\rho_a \nu_w^2}{\rho_w \nu_a^2}, \end{aligned}$$

since the following relation is satisfied under the conditions of Reynolds number similitude.

Table 1 Conditions based on Reynolds number similitude

	Actual condition	Experimental condition
Arm thickness (mm)	1	10
Temperature (°C)	45	10
Kinematic viscosity (m ² /s)	1.77×10^{-5}	1.31×10^{-6}
Reference flow velocity (Rotation speed) (m/s)	40	0.3
Reynolds number	2.3×10^3	2.3×10^3

$$\frac{U_a d_a}{\nu_a} = \frac{U_w d_w}{\nu_w},$$

where F , ρ express the force on a carriage arm, fluid density, respectively, and the subscript of a and w expresses the values in the air and water, respectively.

Schematic of the series of the experiments is shown in Fig. 2. Firstly, the experiments were done in a uniform cross flow to investigate overall characteristics of the flow around the carriage arm. Secondly, the effects of velocity profile of incident flow, installation angle of the arm and misalignment of the arm position were investigated. Finally, the effect of the configuration of the trailing edge of the carriage arm was examined to reduce the dynamic lift force on the arm.

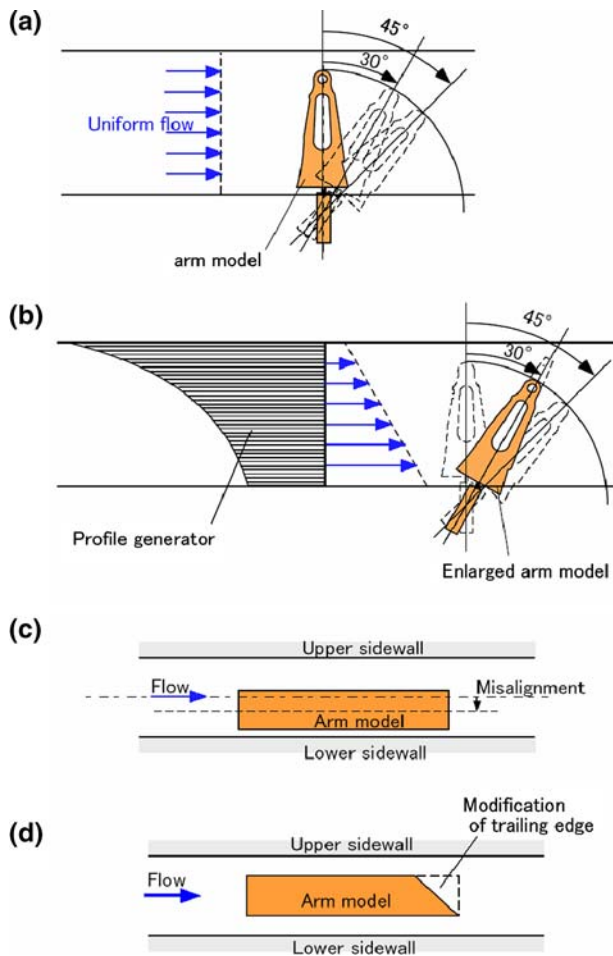


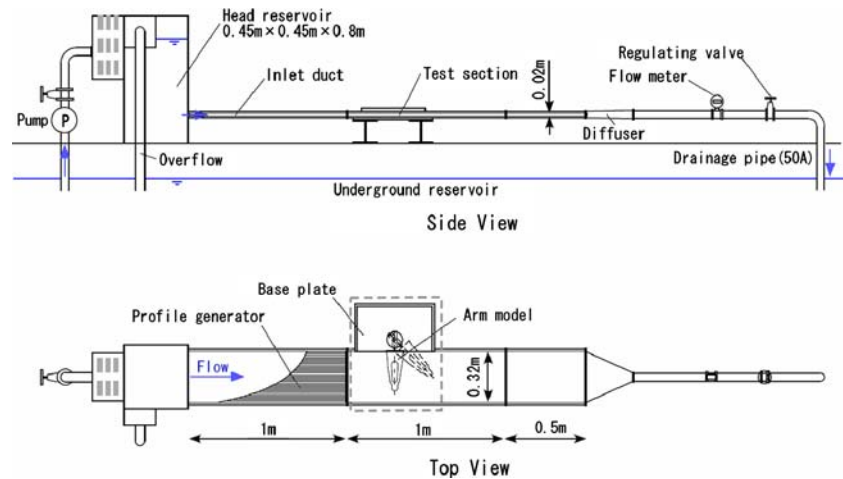
Fig. 2 Schematic of the series of the experiments. **a** Basic case. **b** Experiments on the effect of incidence profile. **c** Experiments on the effect of misalignment. **d** Experiments on the effect of the arm configuration (45° cutoff of the trailing edge)

2.2 Water test loop

A schematic arrangement of the water test loop used in the experiments is shown in Fig. 3. The loop comprises of an underground reservoir, a head reservoir, an inlet duct, a test section and a drainage pipe. The flow is provided by a pump, and passes through the head reservoir and the inlet duct, and then enters into the test section. The head reservoir has a rectangular cross-section of 0.45 × 0.45 m and a 0.8 m height. The inlet duct for rectification measures 20 mm in height, 320 mm in width and 1 m long in the flow direction. The test section, which comprises of transparent acrylic plates, is also rectangular, 20 × 320 mm in cross section, and 1 m long in the flow direction. The water through the test section is drained to the underground reservoir through the drainage pipe with a diameter of 50 mm. A magnetic flowmeter (Yokogawa, ADMAG AE205SG) and a regulating valve are installed in the middle of the drainage pipe. The flow rate is adjusted by the regulating valve.

It should be noted that a carriage arm in actual HDDs is not subjected to a flow with a uniform velocity profile in the radial direction. According to Abrahamson et al. (1989) and Schuler et al. (1990), the tangential flow velocity between shrouded corotating disks depends on the dimensionless radius defined as r/R where r and R denotes the distance from the disk center and the radius of the disk, respectively. They have shown that the tangential flow velocity almost coincide with the local disk speed where r/R is less than about 0.65 while it is lower than the local disk speed and is fairly constant where r/R is larger than about 0.65. Barbier et al. (2006) have obtained similar results by experiments with larger scale model concerning flow velocity profile of 3.5 in. HDDs. To simulate these velocity profiles in the water experiments, a special profile generator of honeycomb type is designed and is installed in the inlet duct. Each flow path of the honeycomb is rectangular, about 4 × 4 mm in cross section. The length of each flow path is varied to control the friction loss. Figure 4a shows the local disk speed in actual 3.5 in. HDDs. Figure 4b shows velocity profiles in the water tests equivalent to the local disk speed in the actual HDDs based on Reynolds number similitude. Figure 4c shows a typical result of preliminary measurement of velocity profile of water flow into the test section. Time-averaged local flow velocity was measured by an electromagnetic current meter (Tokyo-keisoku, SFT-200-05) in cases with and without the profile generator. Flow rate through the test section is 121 l/min. in both cases. In the case without profile generator, the profile of flow velocity is almost flat

Fig. 3 Schematic arrangement of water test loop



except for in the vicinity of side wall. On the other hand, a linear velocity profile is achieved at $z < 240$ mm in the case with the profile generator, and the flow is decelerated in the vicinity of side wall. The profile is fairly similar as those in shrouded corotating disks obtained by previous studies.

Photographs of the water test loop, test section and profile generator are shown in Fig. 5.

2.3 Arm model and fluid force measurement

Figure 6 shows schematic of the ten times enlarged arm model (we call this original model “Model #1”) fixed on the base plate. An arm model section and a support section are in one piece, and are made of aluminum. The arm model section simulates the outer shape of a major part of a typical carriage arm equipped on 3.5 in. HDDs. A suspension and a slider are not simulated. The support section consists of a cylindrical section with an 8 mm diameter and a 16 mm length, and a rectangular section with a 10 mm thickness, a 30 mm width and a 104 mm length. Two bolts are used to fix the rectangular section on the base plate. Four water-proof strain gauges are attached to the surface of the cylindrical section to form a Wheatstone bridge for measuring the force on the arm in each of the drag, lift and torsional directions. Dynamic strain amplifiers (Kyowa, DPM-71A) are used, and their outputs are recorded by a digital data recorder (Teac, DR-M3bMK2). In preliminary calibration tests of the strain gauges, a weight was hung from the tip of the arm, and the outputs of strain gauges were correlated to the magnitude of the bending moment and torque. The natural frequency of the cantilevered arm in the water is about 50 Hz according to the hammering tests.

To investigate the effect of trailing edge shape on the fluid force, another model (“Model #2”) is also

used. The trailing edge is cut off at the angle of 45° . Figure 7 shows the photographs of the enlarged arm models.

2.4 Flow visualization test

Figure 8 is a schematic arrangement of the flow visualization tests. A fluorescent dye is injected through four dye outlet ports, each with a diameter of about 2 mm. The injected dye is advected by the flow around the arm and illuminated by a laser light sheet. The flow patterns visualized by the dye injection are taken from both top and side views by a high-speed CCD camera (nac, MEMRECAM Ci). The frame rate in the tests is 500 frame per second.

3 Experimental results

3.1 Identification of primary mechanism of fluid excitation

The experiments described above were done first in a uniform cross flow in order to identify excitation mechanism by fluid dynamic phenomena and frequency characteristics of the fluid dynamic force acting on the arm.

Figure 9 shows the power spectral densities (PSDs) of the bending moment in the drag and lift directions and fluid dynamic torque at the cylindrical support. Installation angle of the arm is 0° and the incident flow velocity is 0.27 m/s (almost equivalent to 10,000 rpm in the actual HDDs). Predominant spectrum peak at 6.5 Hz (equivalent to about 8 kHz in the air) can be seen in the PSD of the bending moment in the lift direction. Figure 10 shows the effect of the incident flow velocity on PSDs of the bending moment in the lift

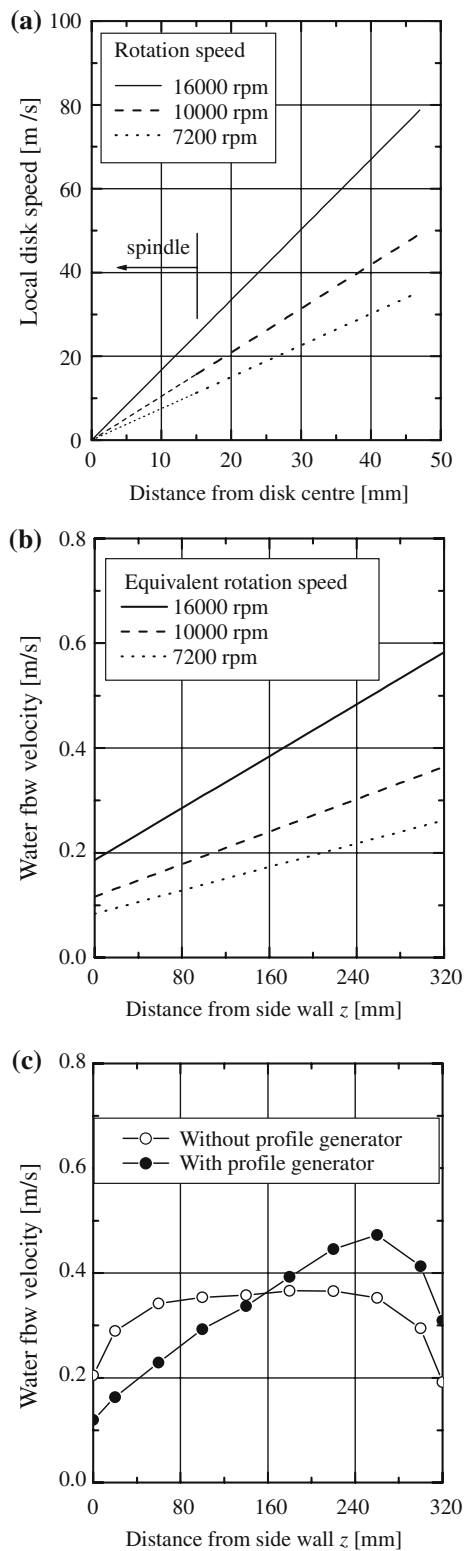


Fig. 4 Comparison of flow velocity profiles. **a** Local disk speed in actual HDDs. **b** Equivalent velocity profile in water experiments based on Reynolds number similitude. **c** Typical result of preliminary measurement of incident flow velocity into test section with and without profile generator

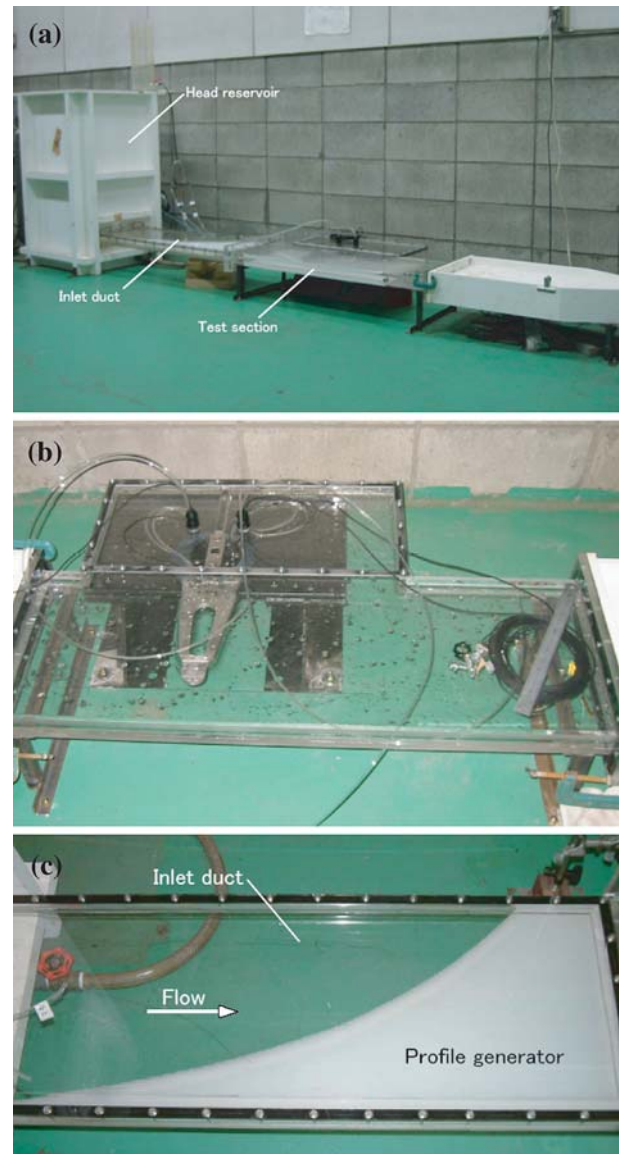


Fig. 5 Photographs of water test loop and profile generator. **a** Water test loop. **b** Test section. **c** Profile generator

direction. The installation angle of the arm is 0° . The amplitude of the spectral peak rapidly increases as the incident flow velocity increases. The rapid increase is reasonable since the amplitude of the fluid force is generally proportional to ρU^2 and that of PSD is proportional to $(\rho U^2)^2$. The frequency of the peak is almost proportional to the incident flow velocity. Hence, we introduce the Strouhal number St defined as follows:

$$St = f_s d/U,$$

where f_s denotes the frequency of the predominant spectral peak. We can find that St is about 0.24.

Fig. 6 Ten times enlarged arm model fixed on base plate. Dimensions in millimeters

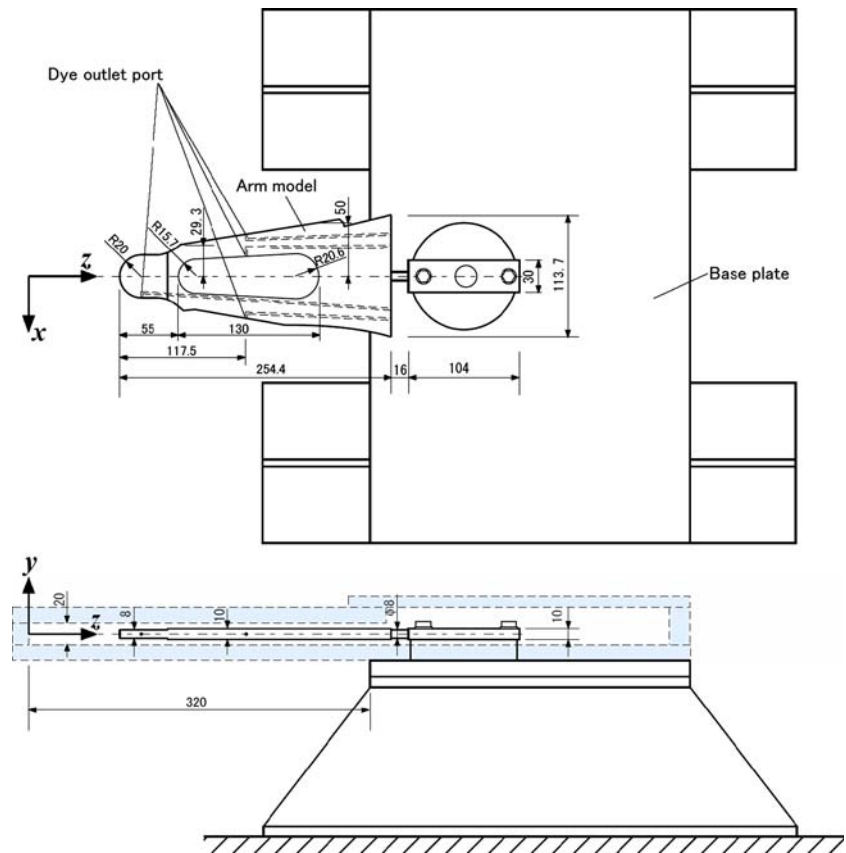


Figure 11 shows the effect of the installation angle of the arm on PSDs of the bending moment in the lift direction. The graph shows that the amplitude of the spectral peak dramatically decreases as the installation angle increases. The peak almost disappears in the case of the installation angle of 45° .

Figure 12 shows typical vortex flows observed around the arm subjected to a uniform cross-flow in the same condition as in Fig. 9. These vortical flow patterns possibly cause fluid excitation force on the arm. These photographs were taken from the tip side of the arm model as shown in Fig. 8a. Alternate vortex shedding from the trailing edge can be clearly seen in Fig. 12a. The frequency is approximately 6–7 Hz counted by eye observation of the movie. Small scale vortices shed from upper corner of the arm due to shear flow instability can also be seen in Fig. 12b. The frequency is about 50 Hz (equivalent to 60 kHz in the air). Figure 13 shows photographs taken from the upper side of the test section as shown in Fig. 8b. Disturbed flow behind the tip of the arm can be observed in case of the installation angle of 0° while small scale vortex street can be observed in the shear flow separated from the tip of the arm in case of the installation

angle of 45° . The frequency is about 30 Hz (equivalent to 40 kHz in the air).

Among these vortical flows, the frequency of alternate vortex shedding from the trailing edge corresponds well to that of the spectral peak found in Fig. 9. These results indicate that the dynamic lift with the spectrum peak of $St = 0.24$ originates from the alternate vortices in the wake of the arm. On the other hand, small scale vortices due to shear flow instability probably do not generate a considerable fluid excitation force which causes arm vibration. However, small scale vortices in the shear flow separated from the arm tip may cause vibration of a suspension and slider if they impinge on a suspension and slider.

3.2 Effects of parameters on PSD of dynamic lift force

Figure 14 shows the effect of oncoming flow profile. The graph shows the PSDs of the bending moment in the lift direction with and without the profile generator, where the installation angle of the arm is 0° and the velocity profiles are the same as shown in Fig. 4c. The results show that the PSDs look almost the same level

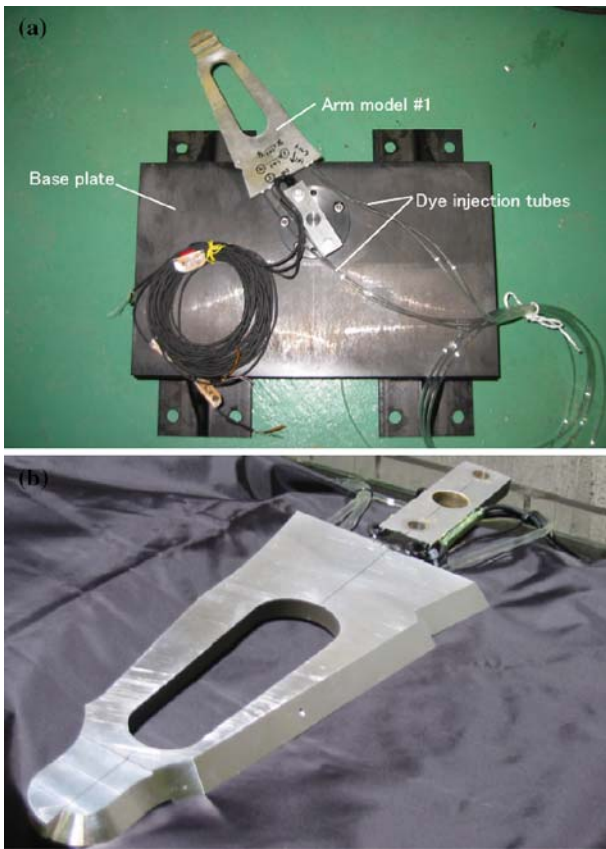


Fig. 7 Photographs of enlarged arm model. **a** Original model #1 fixed on base plate. **b** Modified model #2

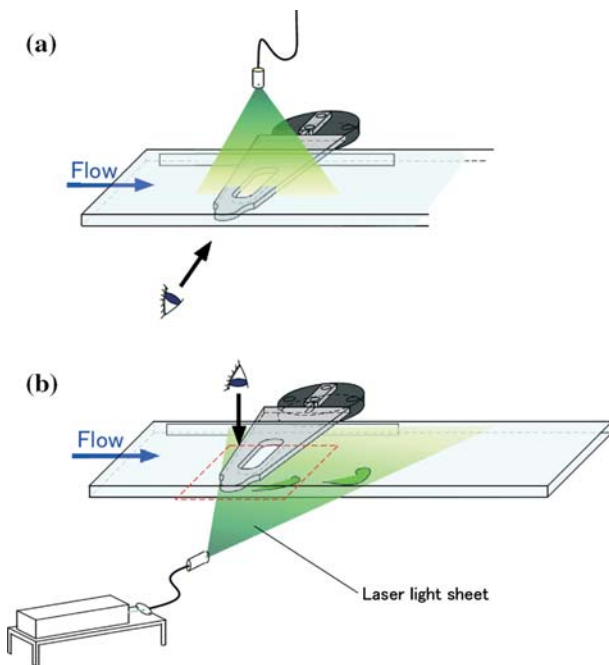


Fig. 8 Schematic arrangement of flow visualization tests. **a** Side view. **b** Top view

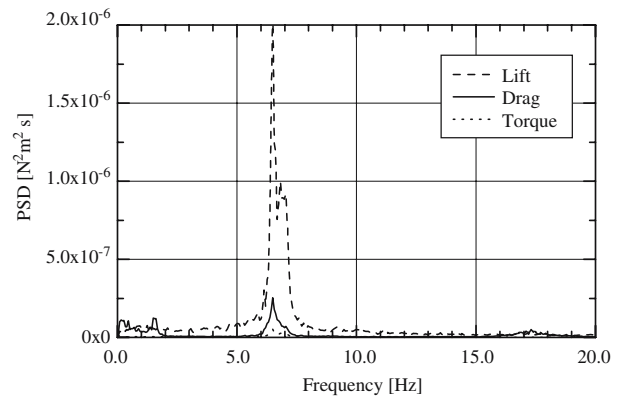


Fig. 9 PSDs of bending moment in the drag and lift directions and fluid dynamic torque. Incident flow velocity is 0.27 m/s. Installation angle of arm is 0°

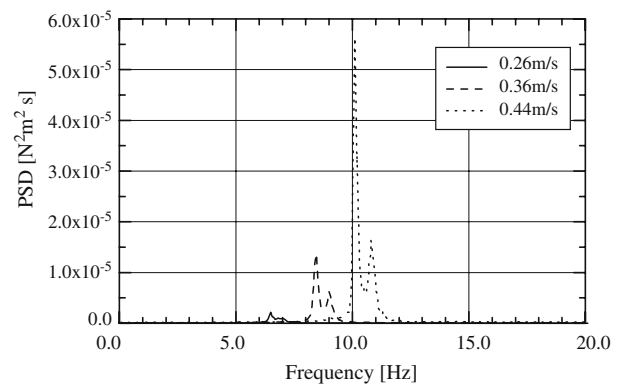


Fig. 10 Effect of incident flow velocity on PSDs of bending moment in the lift direction. Installation angle of arm is 0°

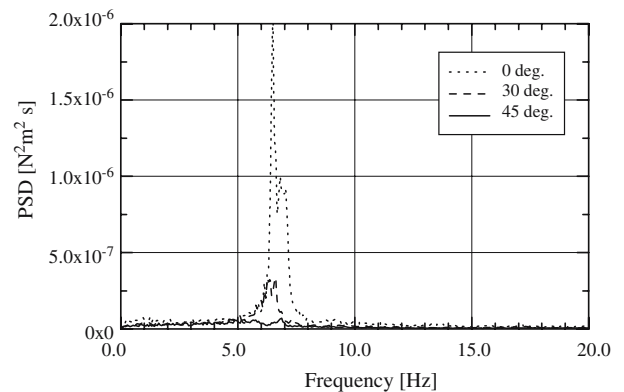


Fig. 11 Effect of installation angle of arm on PSDs of bending moment in the lift direction. Incident flow velocity is 0.27 m/s

in both cases. Figure 15 shows the flow patterns observed in the case with the profile generator. A similar flow pattern of alternate vortex shedding as that in Fig. 12a can be seen. Figure 16 shows comparison of

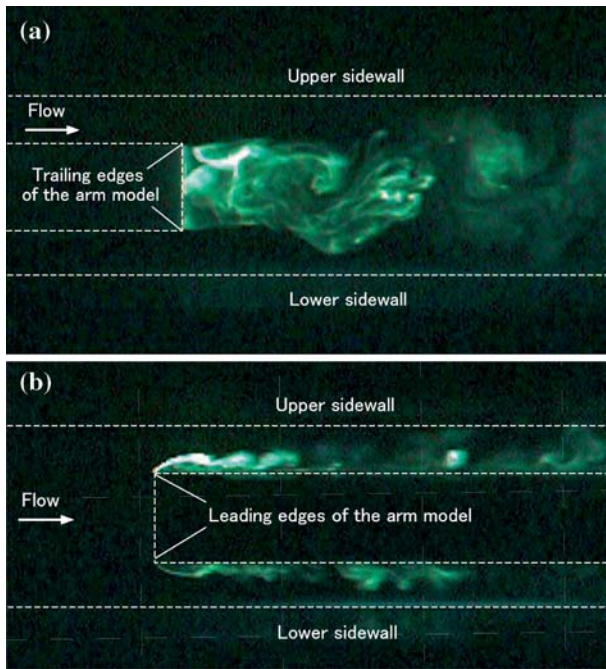


Fig. 12 Typical vortex flow patterns around arm model subjected to uniform cross flow. Incident flow velocity is 0.27 m/s. **a** Alternate vortex shedding from trailing edges. **b** Leading edge vortices due to shear layer instability

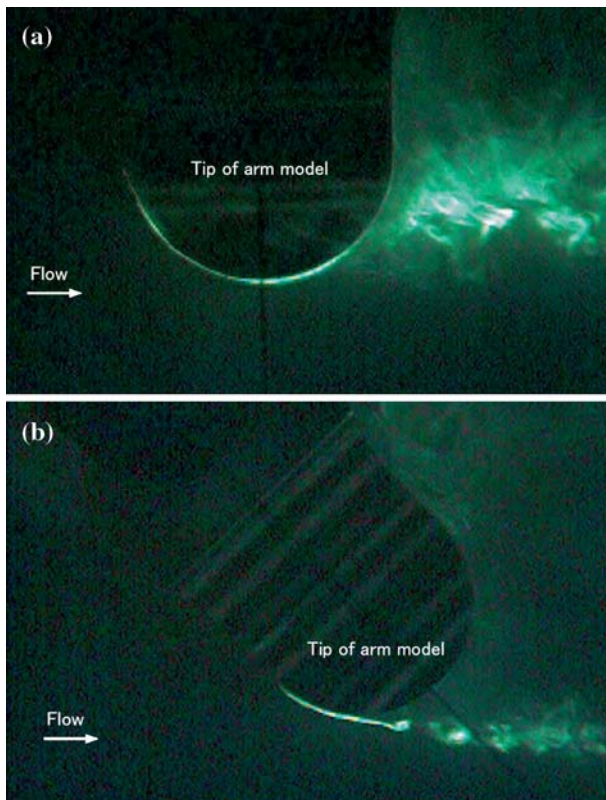


Fig. 13 Flow patterns around tip of arm model. Incident flow velocity is 0.3 m/s. **a** Installation angle of arm is 0°. **b** Installation angle of arm is 45°

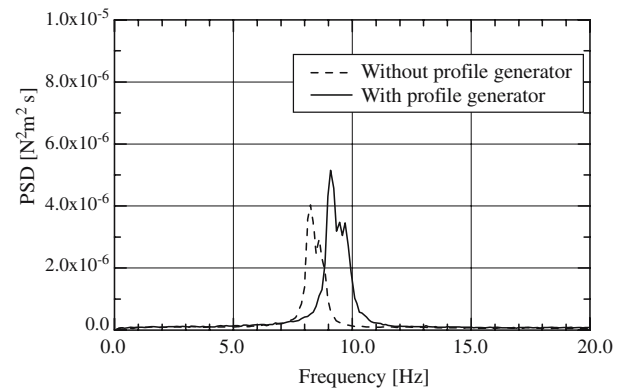


Fig. 14 Effect of velocity profile of incident flow on PSD of bending moment in the lift direction. Installation angle of arm is 0°

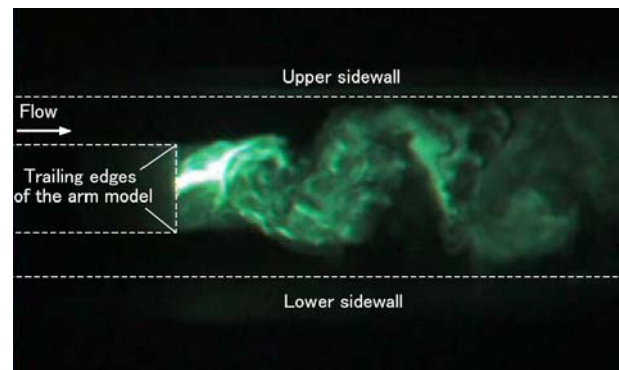


Fig. 15 Alternate vortex shedding from trailing edges in case with profile generator. Installation angle of arm is 0°

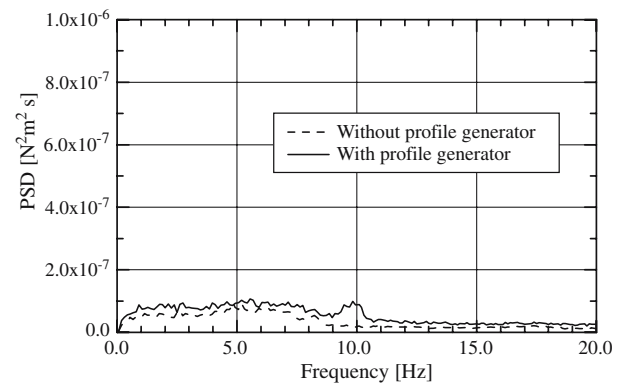


Fig. 16 Effect of velocity profile of incident flow on PSD of bending moment in the lift direction. Installation angle of arm is 45°

the PSDs of the bending moment in the lift direction with and without the profile generator in the case of the installation angle of 45°. No remarkable difference between the PSDs can be seen. These results indicate

that the profile of the incident flow velocity has little effect on the flow around and the fluid force on the arm.

Figure 17 shows the effect of misalignment of the arm on the PSD. Misalignment of the arm in the gap direction is 2 mm (equivalent to 200 μm in the actual HDDs). The installation angle of the arm is 0° and the profile generator is used. The PSDs look similar to each other though slight increase in the amplitude of the spectral peak can be seen in the case with misalignment. Figure 18 shows the results in the cases that the installation angle of the arm is 45° . No remarkable difference between the PSDs can be seen. These results indicate that misalignment of the arm position in the gap direction has little effect on the flow around and the fluid force on the arm.

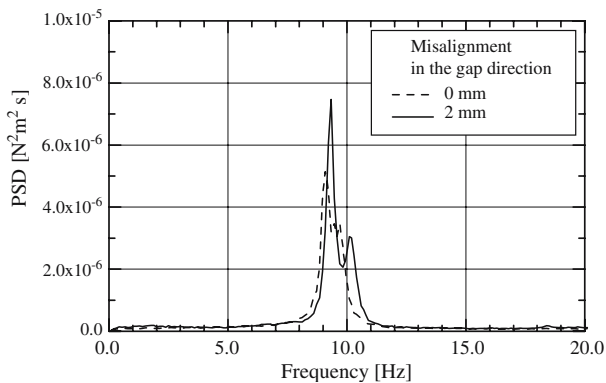


Fig. 17 Effect of misalignment of arm in the gap direction on PSD of bending moment in the lift direction. Installation angle of arm is 0°

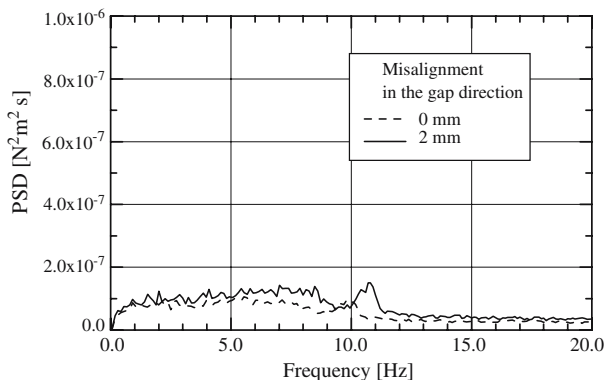


Fig. 18 Effect of misalignment of arm in the gap direction on PSD of bending moment in the lift direction. Installation angle of arm is 45°

3.3 Effect of arm configuration on PSD on dynamic lift force

The effect of the configuration of the trailing edge on the PSD was also investigated to reduce the dynamic lift force on the arm. Figures 19 and 20 shows comparison of the PSDs of the bending moment in the lift direction on the model #1 and #2. The installation angle of the arm is 0° . It is clearly seen that model #2 decreases PSD level.

In the case of 30° , however, small effect is found since the peak level in the PSD of model #1 is not so large, compared with the case of 0° .

4 Conclusion

Flow visualization tests and fluid force measurements were conducted in a water tunnel with ten times

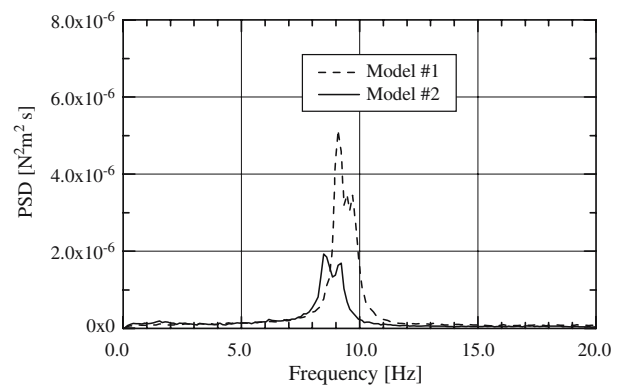


Fig. 19 Effect of configuration of trailing edge on PSD of bending moment in the lift direction. Installation angle of arm is 0°

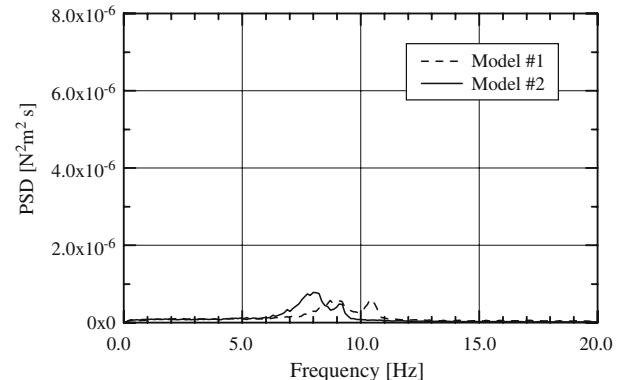


Fig. 20 Effect of configuration of trailing edge on PSD of bending moment in the lift direction. Installation angle of arm is 30°

enlarged models of an actual carriage arm equipped on HDDs under Reynolds number similitude to identify the excitation mechanism by fluid dynamic phenomena and frequency characteristics of the fluid dynamic force on the arm. The effects of the incident flow velocity and profile, the installation angle and position, the configuration of the trailing edge of the arm on the power spectral density of the bending moment in the lift direction were also investigated.

The new findings obtained from the experiments are summarized as follows:

- (1) There exist four kinds of vortex flow patterns around the arm such as;
 - (a) Trailing edge vortex (TEV): alternating vortices in the wake of the carriage arm (St is about 0.24),
 - (b) Leading edge vortex (LEV): small scale vortices shed from the leading edges of the carriage arm due to shear flow instability,
 - (c) Tip vortex 1(TV1): disturbance due to the flow wrapping around the tip of the carriage arm,
 - (d) Tip vortex 2(TV2): small scale vortices in the shear flow separated from the arm tip in the cases that the installation angle is not zero.
- (2) Predominant spectrum peak found in the dynamic lift force on the arm originates from the alternate vortex shedding from the trailing edges, the Strouhal number of which is about 0.24. The amplitude of the spectral peak dramatically decreases as the installation angle of the arm increases. The peak almost disappears in the case of the installation angle of 45° .
- (3) The profile of the incident flow velocity and the position of the arm in the gap direction have little effect on the flow around and fluid dynamic force on the arm.
- (4) Dynamic lift can be reduced by modification of trailing edge shape of the arm. The effect of

cutoff of the trailing edge, however, is not so large in the case that the installation angle is 30° .

Acknowledgments This work was performed under the support of SRC from 2003 to 2006.

References

- Abrahamson SD, Eaton JK, Koga DJ (1989) The flow between shrouded corotating disks. *Phys Fluids A* 1(4):241–251
- Barbier C, Humphrey JAC, Maslen E (2006) Experimental study of the flow in a simulated hard disk drive. *J Fluids Eng* 128:1090–1100
- Eguchi Y, Nishihara T, Tanaka N (1998) Boundary layer structure around an electric wire designed for wind force reduction. In: Proceedings of the ASME fluids engineering division summer meeting, FEDSM98-4895, Washington DC
- Eguchi Y, Kikuchi N, Kawabata K, Yukino T, Ishikubo Y (2002) Drag reduction mechanism and aerodynamic characteristics of a newly developed overhead electric wire. *J Wind Eng Ind Aerodyn* 90:293–304
- Gao F, Yap FF, Yan Y, Harmoko H (2006) Shock analysis of non-operating hard disk drives based on a multibody dynamic formulation. *Microsyst Technol* 12:247–257
- Jiang L, Miles RN (1999) A passive damper for the vibration modes of the head actuator in hard disk drives. *J Sound Vib* 220(4):683–694
- Kubotera H, Tsuda N, Tatewaki M, Maruyama T (2002) Aerodynamic vibration mechanism of HDD arms predicted by unsteady numerical simulations. *IEEE Trans Magn* 38(5):2201–2203
- Schuler CA, Usry W, Weber B, Humphrey JAC, Greif R (1990) On the flow in the unobstructed space between shrouded corotating disks. *Phys Fluids A* 2(10):1760–1770
- Shimizu H, Shimizu T, Tokuyama M, Masuda H, Nakamura S (2003) Numerical simulation of positioning error caused by air-flow-induced vibration of head gimbals assembly in hard disk drive. *IEEE Trans Magn* 39(2):806–811
- Tsuda N, Kubotera H, Tatewaki M, Noda S, Hashiguchi M, Maruyama T (2003) Unsteady analysis and experimental verification of the aerodynamic vibration mechanism of HDD arms. *IEEE Trans Magn* 39(2):819–825
- Xu LM, Guo N (2003) Modal testing and finite element modeling of subsystem in hard disk drive. *Mech Syst Signal Processing* 17(4):747–764